Journal of Photochemistry & Photobiology, A: Chemistry 406 (2021) 113005

Contents lists available at ScienceDirect

Journal of Photochemistry & Photobiology, A: Chemistry

journal homepage: www.elsevier.com/locate/jphotochem

Polyaniline supported $CdS/CeO_2/Ag_3PO_4$ nanocomposite: An "A-B" type tandem n-n heterojunctions with enhanced photocatalytic activity

Abi M. Taddesse [a,*], Tigabu Bekele [a], Isabel Diaz [b], Abebaw Adgo [c]

[a] Department of Chemistry, Haramaya University, Haramaya, Ethiopia
[b] Instituto de Catálisis y Petroleoquímica, CSIC, c/Marie Curie 2, Madrid 28049, Spain
[c] Chemistry Department, Bahir-Dar University, Addis Ababa, Ethiopia

ARTICLE INFO

Keywords:
Degradation
Immobilization
Methyl orange
Nanocomposite
Photocatalysis
Polyaniline

ABSTRACT

In the present work, ternary composites of the form $CdS/CeO_2/Ag_3PO_4$ with $CdS:CeO_2/Ag_3PO_4$ molar ratios of (1:1, 2:1, 3:1 and 4:1) were synthesized by co-precipitation method. Polyaniline supported $CdS/CeO_2/Ag_3PO_4$ nanocomposite was also synthesized by "*in situ*" chemical oxidative method. Physicochemical properties of the photocatalyst materials were determined using XRD, BET, SEM-EDX, TEM, UV/Vis, FTIR and PL techniques. Photocatalytic activities of the ternary $CdS/CeO_2/Ag_3PO_4$ (1:1, 2:1, 3:1 and 4:1 molar ratios) nanocomposites were found to be higher than their single and binary counterparts. The effects of different operational parameters such as pH, initial dye concentration, photocatalyst load and scavengers in MeO dye degradation study confirmed the following optimum values: pH 4, initial dye concentration 10 ppm and photocatalyst load 0.15 g/L. The effects of different scavengers suggest that $\bullet O_2^-$ and $\bullet OH$ scavengers play major roles in the degradation of MeO. The supported photocatalyst exhibited a relatively higher efficiency (93.4%) on the photodegradation of MeO dye. In addition, it showed fairly well photocatalytic activity (70.7%), for the textile effluent collected from one of the local textile industries. Furthermore, the reusability of the supported photocatalyst was tested. About 80% of the catalyst efficiency was maintained after four successive runs exhibiting the potential application of this novel composite for degradation of MO dye from aquatics system.

1. Introduction

Azo dyes are among the largest family of textile dyes covering about 70% of all textile dyes currently employed. In the process of dyeing of the fabric, nearly 80% of dye and associated chemical molecules from dye mixtures are adsorbed [1,2]. The remaining 20% of the dye is wasted due to limited sorption capacity of the fabric to be colored. Majority of the azo dyes are toxic, carcinogenic [3]. Azo dyes are resistant to biodegradation due to their chemical structure. Besides, biodegradation of these dyes can generate amine by-products that can be harmful and carcinogenic [4]. Hence, complete destruction of dyes into innocuous products from waste water is the major concern towards environmental pollution abatement.

Plenty of methods have been employed to eradicate dyes from waste waters so as to reduce their environmental impact. These techniques can be categorized as physical, chemical, biological and recently additional classifications as acoustical, radiation and electric processes [5]. However, dyes are highly recalcitrant to degradation because of their intricate chemical structures. For instance, chemical and physical methods are nondestructive; they either decrease the dye concentration or transfer the same from aqueous phase to solid phase thereby creating secondary pollution [6]. The necessity of state of the art approaches such as advanced oxidation processes that are capable of destroying recalcitrant dye effluents is imperative. Photocatalysis is a "green" technology based on abundant natural resources such as solar energy and oxygen from air that occurs at ambient temperature and pressure. The efficiency of this technique for the abatement of dyes and other organic chemicals could be attributed to the fact that the photocatalytic materials employed are non-toxic, relatively inexpensive, have high surface area and broad absorption spectra ranging from ultraviolet to visible region [7].

Cerium dioxide (CeO_2), as a fascinating rare earth material, has attracted a great deal of attention owing to its promising photoactivity, cost effectiveness, physical and chemical stability, high oxygen storage capacity with abundant oxygen vacancies (Vo), excellent catalytic property due to the reversible Ce^{3+}/Ce^{4+}pairs, resistance to

* Corresponding author.
E-mail address: abi92003@yahoo.com (A.M. Taddesse).

https://doi.org/10.1016/j.jphotochem.2020.113005
Received 25 July 2020; Received in revised form 21 October 2020; Accepted 26 October 2020
Available online 1 November 2020

photocorrosion and environmentally friendly properties [8,9,10]. Nevertheless, pure CeO_2 can only be excited by ultraviolet light (UV) because of its wide band gap (2.8-3.4 eV) [9,10,11] and could only absorb the UV region, which is less than 5% of the solar spectrum thereby restricting its application. In order to highly utilize solar energy, various methods such as metal/nonmetal doping, noble metal deposition, forming composites [10,12], construction of solid solutions [10] and doping-coupling [13,14] have been designed to enhance the absorption of CeO_2 photocatalysts in the visible light region

Among the various methods to modify wide band gap semiconductors, coupling with narrow band semiconductors is an effective strategy [8]. Visible light sensitization of CeO_2 could be occurred in either of the two ways to get "Type-A" or "Type-B" binary heterojunctions depending on the flat band potentials of the narrow band gap semiconductors. If the conduction band (CB) level of the semiconductor sensitizer is located relatively higher than that of CeO_2, as in the case of CdS/CeO_2 [15,16], the electrons photogenerated by the sensitizer are more reducing on account of the more negative CB of the sensitizer (CdS). As the result, electrons are transferred to the CB of CeO_2, and these photo-excited electrons can initiate many reduction reactions. This kind of coupling can be classified as "Type-A heterojunction" but considered less effective due to hindered complete oxidation of organic pollutants to CO_2 and H_2O. On the other hand, if the valence band (VB) level of the sensitizer is located lower than that of CeO_2, as in the case of Ag_3PO_4/CeO_2 [17], the visible-light sensitization can induce the hole-transfer from the sensitizer to the host semiconductor, CeO_2. In this case, holes can be generated in the VB of CeO_2, initiating in turn various oxidation reactions. Considering the sturdy oxidative ability of the holes in the VB of CeO_2, efficient oxidation of organic compounds is expected to this system under visible-light (denoted as Type-B heterojunction) [18,19].

Construction of CeO_2-based ternary systems has received increasing attention in virtue of multiple properties, which came from the synergistic effects of different individual components and resulted in outstanding photocatalytic behaviors [20]. In view of this fact, we hypothesized formation of ternary hetrojunction of the form "A-B Type" by combining "A type" and "B-Type" hetrojunctions that could lead to better photocatalytic activity as the photogenerated electrons and holes would be expected to be effectively separated. Extensive reports have been made evidencing better photocatalytic activities of ternary systems comprising ZnO as host semiconductors [21,22,23] compared with their binary counterparts. However, there is little information on fabrication of ternary composites considering CeO_2 as a host semiconductor [10,11, 24]. To the best of our knowledge, there has been no report on the synthesis and characterization of an "A-B Type" heterojunction based on $CdS/CeO_2/Ag_3PO_4$ nanocomposite for photocatalytic application.

On the other hand, employing bare or unsupported nanomaterials is being discouraged due to problem of ecotoxicity. As the result, several attempts have been made to improve the degradation efficiency and recyclability of the nanophotocatalysts using suitable supports. Among others, polyaniline has been successfully used to load various nanoparticles. It is evidenced that immobilizing nanomaterials onto polyaniline expanded the absorption range further in the visible region, and promoted the effective separation of photo-excited electron-hole pairs; thereby enhancing the photocatalytic efficiency [25,26,27]. The objective of the present work was to synthesize polyaniline supported $CdS/CeO_2/Ag_3PO_4$ nanocomposite and evaluate its photocatalytic activity for degradation of model pollutant azo dye, Methyl orange (MeO). In addition, the decolorization efficiency of the as synthesized photocatalytic material was also conducted on effluent collected from textile company situated in Bahir Dar City, Ethiopia.

2. Experimental

2.1. Materials

All the chemicals and reagents used were of analytical grade and used with no further purification.

2.2. Preparation of photocatalysts

2.2.1. Synthesis of single (CeO_2, CdS, Ag_3PO_4) nanoparticles

Pristine cerium oxide nanoparticles were prepared by precipitation method following a modified approach [28]. In a typical procedure, 0.1 M of cerium nitrate hexahydrate $Ce(NO_3)_3.6H_2O$ was prepared in 100 mL of deionized water. Aqueous NH_4OH solution was added dropwise into the above solution containing cerium precursor and stirred until precipitation was formed. The stirring was continued for another 2 h and the reaction condition was maintained at pH = 10. The reaction mixture was then stirred for additional 12 h to complete the precipitation process. The resulting yellow colored slurry was decanted, filtered and washed three times each with deionized water and ethanol. The precipitate was oven dried at 140 ℃ for 12 h and calcined at 500 ℃ for 3 h to get CeO_2 nanoparticles (C1). Ag_3PO_4 nanoparticle was synthesized by a simple precipitation method [29]. In this method, equal molarity (0.1 M) of $AgNO_3$ and Na_2HPO_4 were dissolved in 60 mL distilled water separately. Then Na_2HPO_4 solution was dropped into $AgNO_3$ solution under continuous magnetic stirring for 4 h. The resulting yellow precipitate was collected, washed and dried in an oven at 60 □ for 6 h and the final precipitate was calcined at 300 ℃ for 2 h to get Ag_3PO_4 nanoparticle (C2). In the synthesis of CdS nanoparticles, equal molarity (0.1 M) $Cd(CH_3COO)_2.4H_2O$ and $Na_2S.9H_2O$ solutions were prepared in separate beakers. Then the solution containing sodium sulfide was dropped into cadmium precursor solution through continuous stirring for 2 h at room temperature. During the reaction, nitrogen gas was continuously purged into the suspension. Then, the yellow precipitate formed was collected centrifuged and washed three times with deionized water and ethanol to remove the residue. The product obtained was finally dried at 70 ℃ for 5 h [30] followed by calcination at 300 ℃ for 2 h in a furnace to get CdS nanoparticles (C3).

2.2.2. Synthesis of binary (CdS/CeO_2, Ag_3PO_4/CeO_2) nanocomposites

In a typical procedure, 0.1 M of the as-synthesized CeO_2 powder was dispersed in 100 mL of distilled water and sonicated for 30 min, then 0.1 M of $Cd(CH_3COO)_2.4H_2O$ was added. After 1 h of stirring, 0.1 M $Na_2S.9H_2O$ solution was added slowly into the above solution. The precipitate formed was filtered and washed with distilled water and ethanol several times, dried in an oven at 60 ℃ for 24 h to obtain CdS/CeO_2 nanocomposite (CC1) [31]. The preparation of Ag_3PO_4/CeO_2 binary composite was carried out by an *in situ* precipitation method [32]. In a typical synthesis, 0.0814 mmol of the as-prepared CeO_2 nanoparticle was dispersed in 100 mL of deionized water and sonicated for 30 min, followed by addition of 0.1 M of $AgNO_3$ aqueous solution. The mixture was stirred for 30 min. To this mixture solution, 0.1 M Na_2HPO_4 solution was added dropwise with stirring for another 2 h. Then the color of the solution was changed from white to yellow. The precipitate formed was filtered and washed three times with deionized water and ethanol. Finally, the product obtained was dried in an oven at 80 ℃ for 10 h (CC2).

2.2.3. Synthesis of ternary $CdS/CeO_2/Ag_3PO_4$ nanocomposite

Synthesis of the ternary nanocomposites was performed taking appropriate amount of the as-synthesized binary CeO_2/Ag_3PO_4 composite powder by varying the amount of CdS. In a typical procedure, 0.1 M of CeO_2/Ag_3PO_4 powder was dissolved in 100 mL deionized water and sonicated for 2 h. Immediately after sonication, 0.1 M of $Cd(CH_3COO)_2.4H_2O$ was added and the solution was sonicated for another 1.5 h. Aqueous solution of $Na_2S.9H_2O$ (0.1 M) was dropped into the

above solution through continuous stirring for 3 h. The resulting product was assumed as $CdS/CeO_2/Ag_3PO_4$ nanocomposite and done in four molar ratios (1:1, 2:1, 3:1 and 4:1) [CdS: CeO_2/Ag_3PO_4]. During the reaction, the yellow solution was changed into blue black. Upon filtration, the precipitate was separated out, washed three times with deionized water and ethanol and then dried in an oven for 12 h at 100 ℃ and calcined at 200 ℃ for 2 h. The obtained powder was then ground to get fine particles labeled as CCA1, CCA2, CCA3 and CCA4 for the respective molar ratios (1:1, 2:1, 3:1 and 4:1) of [CdS: CeO_2/Ag_3PO_4].

2.2.4. Polyaniline supported $CdS/CeO_2/Ag_3PO_4$ composite

A typical oxidative polymerization method was adopted for polymerization of aniline in the presence of the as-synthesized nanoparticles [33,34]. For the preparation of polyaniline supported $CdS/CeO_2/Ag_3PO_4$ nanocomposite, equal molarity (0.1 M) of aniline and HCl were dissolved and stirred for 20 min. Then, 2 g of $CdS/CeO_2/Ag_3PO_4$ (CCA4) powder was added into the aniline solution and continuously stirred for 30 min. Equal molarity (0.1 M) of $(NH_4)_2S_2O_8$ and HCl were dissolved and added dropwise into the mixture containing CCA4 and aniline while stirred for 1 h. The solution was stirred in an ice bath for another 1.5 h. The gelatinous precipitate formed was allowed to stand for 5 h for polymerization. The precipitate was isolated by filtration, washed with deionized water, ethanol and methanol several times, and dried in an oven at 80 ℃ for 12 h [7]. The color of the solution momentarily changed into dark green. The final powder was labeled as polyaniline supported $CdS/CeO_2/Ag_3PO_4$ (PAST) nanocomposite.

2.3. Characterization

The as-synthesized photocatalysts were examined by XRD using a Philips X'PERT Pro PANalytical diffractometer equipped with an X'Celerator detector and using Cu Kα radiation (λ=1.5418 Å) to identify the crystalline structure or their phase purity, and crystal size was calculated by applying the Scherer equation. The diffraction patterns were recorded in the 2θ values ranging from 4 to 90°. The specific surface area of each of the as-synthesized photocatalyst were calculated from the N_2 adsorption-desorption isotherm at liquid-nitrogen temperature -196 ℃ (77 K) and the micropore surface area were calculated by using the Brunauer-Emmett-Teller (BET) method. The optical absorption spectra and band gaps of the as-synthesized photocatalysts were determined using UV/Vis spectrophotometer. The solid state absorbance of the photocatalyst was measured by scanning over the wavelength range of 200-900 nm. Morphologies and particle distribution of the as-synthesized photocatalyst were determined by scanning electron microscopy using a SEM Hitachi TM1000 with EDX detector and back-scattered detector instrument. From energy dispersive X-ray [EDX, an acquisition time (s) 40.0; process time 3 h; and an accelerating voltage (kV) 15.0)] link with SEM, the elemental percent weight distribution of the as-synthesized sample was determined. High resolution transmission electron micrographs (HRTEM) were obtained on a JEOL 2100 F electron microscope operated at 200 kV equipped with an EDS detector INCA x-sight de Oxford Instruments. The as-synthesized photocatalyst was characterized using FTIR (Spectrum 65, PerkinElmer) instrument. Dry mass of the photocatalyst was thoroughly mixed with a given dry mass of KBr and ground to a fine powder. A transparent disc was formed by applying a pressure in moisture free atmosphere. The IR absorption spectrum was recorded between 400 and 4000 cm^{-1}. Photoluminescence (PL) spectra were measured using RF 5301PC Shimadzu photoluminescence. The spectra were obtained in the range of 250-650 nm.

2.4. Photocatalytic degradation studies

The photocatalytic activity of the as-obtained single, binary, and ternary system nanomaterials was tested for the degradation of aqueous solution of methyl orange (MeO) dye. In a typical photocatalytic experiment, 10 ppm of MeO was mixed with 0.2 g/L of the photocatalyst. The mixture was magnetically stirred for 1 h in the dark to ensure adsorption/desorption equilibrium. Then the suspension was subjected to visible light with continuous stirring using magnetic stirrer and the absorbance was measured in 20 min interval to monitor the reaction of MeO aqueous solution. The light source was tungsten lamp (TORCH) (85 W, 6400 K, 170-240 V/50-60 Hz) positioned parallel to the reactor. The distance between the top of reactor and lamp was 12 cm. During the process air/oxygen was purged into the solution using pipette. Then 10 mL suspension was withdrawn at 20 min interval and centrifuged at 3000 rpm for 10 min. Dye absorbance was determined using UV/Visible spectrophotometer at the λ_{max} of MeO solution. Percent degradation (%) was calculated using the following equation [35].

$$\%\ \text{Degradation} = \frac{C_o - C_t}{C_o}\ \chi\ 100 \quad (1)$$

According to kinetic analyses, it has been found that the photocatalytic degradation of organic pollutants obeys a Langmuir-Hinshelwood mechanism and follows a pseudo-first-order reaction with the photocatalytic degradation rate (r) defined by [36]:

$$r = -dC(t)/dt = k_{obs}C(t) \quad (2)$$

When the concentration is very low, the observed rate constant, k_{obs} (min^{-1}) was determined from the simplified Langmuir-Hinshelwood model as given below [37]:

$$\text{Rate} = \ln(C_t/C_o) = -kt \quad (3)$$

Where k_{obs} is the observed rate constant in min^{-1}, C_t is the absorbance at a given time, C_o is the absorbance at initial time and t (min) is the reaction time. Hence, the linear fit between C_t/C_o and irradiation time demonstrates the photocatalytic degradation rate. A higher k_{obs} value indicates a better photocatalytic activity of an investigated sample.

2.5. Determination of point of zero charge

The point of zero charge was determined using 0.15 g of the as-synthesized photocatalytic materials with 50 mL of 0.01 M of $NaNO_3$ solution, added into each flask and adjusted to various pH ranges from 2-12 using (0.1/1 M) HNO_3 or (0.1/1 M) NaOH solutions. The solutions were equilibrated for 60 min in a mechanical shaker and the initial pH was determined. Then 1 g of $NaNO_3$ was added to the above solution and equilibrated for another 60 min. The final pH was measured and ΔpH [$pH_{final\text{-}initial}$ (Y-axis)] versus pH_{final} (X-axis) was plotted to determine the point of zero charge where the graph intersects the X-axis [38].

3. Results and discussion

3.1. Characterization of photocatalysts

Fig. 1a and b represent the XRD patterns of the as-synthesized photocatalysts. Fig. 1a illustrates the XRD patterns of single and binary systems. For the single system nanoparticles, diffraction peaks observed at scattering angle 2θ 28.61, 33.09, 47.58, 56.45, 59.15, 69.46, 76.76, 79.05 and 88.43 ° represent the cubic fluorite structure of CeO_2[JCPDS: 96-434-3162] [39]. The diffraction peaks shown at 2θ of 20.90, 29.76, 33.29, 36.64, 42.55, 47.82, 52.79, 55.08, 57.37, 61.75, 69.98, 71.96, 73.94, 87.28 and 89.26 ° can be indexed to the body centered cubic structure of Ag_3PO_4 [JCPDS: 96-153-0490] [40] where as the broad peaks observed at 2θ of 24.98, 26.53, 28.20, 36.74, 43.83, 47.89, 51.96, 54.66, 66.96, 69.89, 71.14, 72.28, 75.93, 80.52 and 83.33 ° can be ascribed to the hexagonal greenockite structure of CdS nanoparticle [JCPDS: 96-900-8863] [41]. The XRD patterns of binary CeO_2/Ag_3PO_4 composite is similar to that of the pure Ag_3PO_4, and the diffraction peak positions of Ag_3PO_4 showed no distinct change, which indicates that CeO_2 incorporates into the lattice of Ag_3PO_4. The diffraction peak of

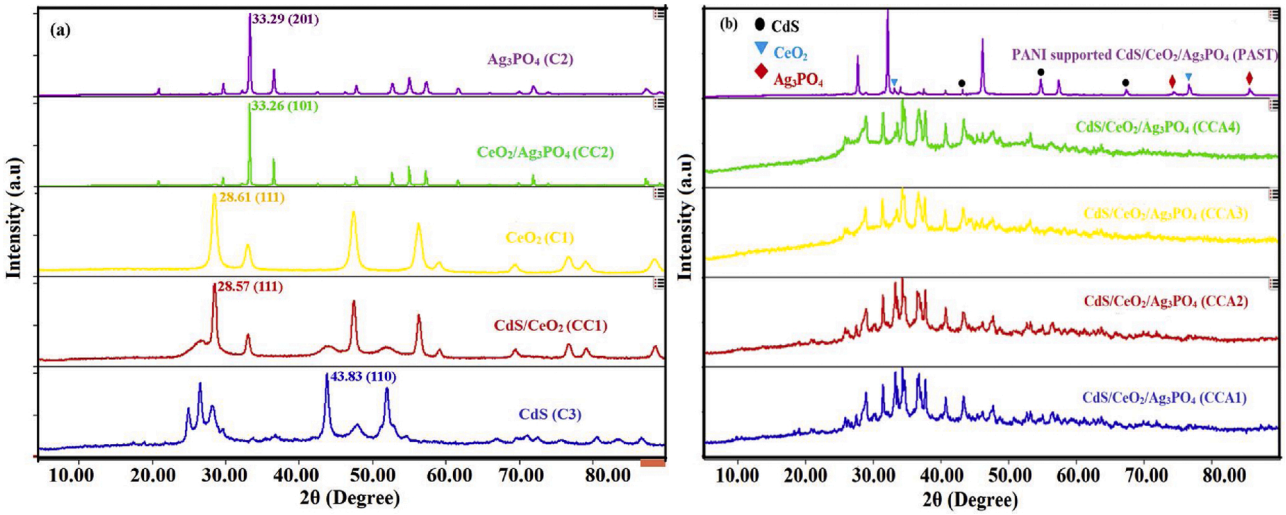

Fig. 1. (a) XRD patterns of Ag_3PO_4, CeO_2/Ag_3P_4, CeO_2, CdS/CeO_2 and CdS photocatalysts; (b) XRD spectra of $CdS/CeO_2/Ag_3PO_4$ (in different composition: CCA1, CCA2, CCA3 and CCA4) and PANI supported $CdS/CeO_2/Ag_3PO_4$ nanocomposite.

CeO_2 appeared very weak intensity in the XRD pattern of the CeO_2/Ag_3PO_4 composite, which might be due to the smaller amount of CeO_2 used during the synthesis [32]. In the case of CdS/CeO_2 binary system, most of the diffraction peaks observed could be ascribed to cubic fluorite structure of CeO_2 nanoparticle. However, weak diffraction peaks at 2θ values of 26.75, 43.83, 52.17 and 69.65° indicate the presence of hexagonal greenockite structure of CdS in the binary system [31,42]. No peak shift was observed between the CeO_2 and CeO_2/Cds revealing the incorporation of CdS in the lattice of CeO_2. Besides, no other phase was observed in the XRD patterns of the binary system, suggesting the purity of the as-obtained composite.

For the ternary systems, four types of composition were formulated just by varying the amount of CdS. In view of that, $CdS:CeO_2/Ag_3PO_4$ molar ratios of 1:1, 2:1, 3:1, and 4:1 were prepared denoted as CCA1, CCA2, CCA3, CCA4 respectively. The XRD patterns for these composites are depicted on Fig. 1b. The general trend showed major diffraction peaks that are more or less similar for all. However, degree of crystallinity is pronounced in the composite where the load of CdS is minimum (1:1). Among the diffraction peaks, 2 θ values of 28.40, 33.04, 47.56 and 56.23 ° could be attributed to the cubic fluorite structure of the crystal CeO_2; peaks at 2θ value of 29.45, 33.19, 33.44, 34.22, 36.61, 53.12 and 70.12 ° represent body centered cubic structure of Ag_3PO_4 whereas peaks at 2θ value of 26.20, 28.14, 28.78, 43.21 and 47.18 ° can be accounted for the hexagonal greenockite structure of CdS nanoparticles. The ternary systems in 4:1 molar ratio (CCA4) was selected for subsequent photocatalytic experiments based on the band gap (Eg) results estimated from the UV/Vis (Table 1) and the preliminary photocatalytic performance (Data not shown). Thus, CCA4 was supported by PANI to fabricate the hybrid material PANI-$CdS/CeO_2/Ag_3PO_4$ (PAST). The supported ternary system, PAST, exhibited less number of diffraction yet more intense peaks compared with bare ternary systems (Fig. 1b). Supporting the ternary system with PANI hence appeared favoring formation of well crystalline nanoparticles. The disappearance of some of the peaks in the supported system could possibly be due to the interaction of $CdS/CeO_2/Ag_3PO_4$ with polyaniline, confirming successful coating of polyaniline over the surface of $CdS/CeO_2/Ag_3PO_4$ (CCA4). The peaks corresponding to 2θ value of 27.79, 31.49, 34.38, 37.70 and 40.70 ° are observed as a result of growth of perpendicular and parallel chains of polyaniline polymer [43] (Fig. 1b).

Table 1
Average crystallite size, specific surface area and band gap of the as-synthesized photocatalysts.

As-synthesized photocatalyst	D (nm)	BET (m2/g)	Band gap (eV)
CeO_2 (C1)	28.61	77.74 ± 0.28	3.26
Ag_3PO_4 (C2)	33.29	0.12 ± 0.00	2.37
CdS (C3)	43.83	26.95 ± 0.08	2.48
CdS/CeO_2 (CC1)	28.57	74.68 ± 0.85	2.23
CeO_2/Ag_3PO_4 (CC2)	33.26	4.75 ± 0.01	2.19
$CdS/CeO_2/Ag_3PO_4$ (1:1), CCA1	34.37	17.33 ± 0.10	2.17
$CdS/CeO_2/Ag_3PO_4$ (2:1), CCA2	34.38	21.83 ± 0.13	2.15
$CdS/CeO_2/Ag_3PO_4$ (3:1), CCA3	34.32	34.52 ± 0.21	2.13
$CdS/CeO_2/Ag_3PO_4$ (4:1), CCA4	34.31	44.72 ± 0.024	2.12
PANI-$CdS/CeO_2/Ag_3PO_4$ (PAST)	32.21	19.49 ± 0.08	2.05

The average crystallite size of each of the as-synthesized photocatalysts [C1, C2, C3, CC1, CC2, CCA (1:1, 2:1, 3:1 and 4:1) and PAST] was calculated using Debye-Scherer formula;

$$D = \frac{K\lambda}{\beta COS\theta} \quad (4)$$

Where, D = crystallite size in nm, K = the shape factor constant taken as 0.9; β is the full width at half maximum (FWHM) in radians, λ is the wavelength of the X-ray (0.15406 nm) for Cu target Kα1 radiation and θ is the Bragg's angle. The estimated average crystallite size of the as-synthesized photocatalysts is found between 10 and 50 nm (Table 1).

The specific surface area of the as-synthesized nanomaterials was determined by the Brunauer-Emmett-Teller (BET) method (Table 1). The specific surface area is largest for CeO_2 (77 $m^2 g^{-1}$) whereas lowest for Ag_3PO_4 (0.122 $m^2 g^{-1}$) showing the compacted nature of the later. The binary system CdS/CeO_2 appeared to have a specific surface area close to CeO_2 (74 $m^2 g^{-1}$). This is in consonant with the result of the XRD (Fig. 1a), as the dominant peaks correspond to CeO_2 in this composite. In the case of CeO_2/Ag_3PO_4, specific surface area close to 4 $m^2 g^{-1}$ was obtained in line with the prevailing peaks representing Ag_3PO_4 in the binary system (Fig. 1a) with very low surface area (0.122 $m^2 g^{-1}$). The specific surface areas of bare (CCA1, CCA2, CCA3, CCA4) and supported ternary nanocomposite (PAST) were found to be 17, 21, 34, 44 and 19.5 $m^2 g^{-1}$ respectively. In general, no specific trend was observed in relation to composition and the specific surface area in all the as-synthesized materials. Besides, the supported ternary nanocomposite showed lower specific surface area compared to its naked counterpart. This is evidenced by well developed peaks demonstrated by the supported system (PAS) as shown on Fig. 1b. Decreased specific surface area of supported nanoparticles is not uncommon; there are similar reports that concur with our findings [44,45]. The role of of PANI in our system is, therefore, appeared to be limited in enhancing the sorption of the dye, rather to yield a composite with decreased band gap shifting further to

the visible region compared to its bare counterparts as evidenced in Table 1.

UV/Vis diffuse absorption edges of the as-synthesized photocatalysts are obtained from plot of absorbance against wavelength. The band gap energy (Eg) of the as-synthesized photocatalysts can be obtained from the equation [15]:

$$Eg = \frac{1240\ \mathbf{eV}}{\lambda_{max}} \quad (5)$$

Where, Eg is band gap energy in eV and λ_{max} is wavelength (nm) corresponding to absorption edge. The optical properties of each of the as-synthesized photocatalyst were investigated by using a UV/Vis diffuse reflectance spectrometer in the range of 200-900 nm. The band gap values of the photocatalysts were determined by analyzing the optical data with the expression for the optical absorbance α and the photon energy hv using Tauc's plot [46,47].

$$\alpha h\nu = A\ (h\nu - Eg)^{n/2} \quad (6)$$

where α is the absorption coefficient, which is proportional to the absorbance, h is the Planck's constant (J.s), *v* is the light frequency (s^{-1}), A is the absorption constant, Eg the band gap energy and n is a constant related to the electronic interband transition. n = 2 for an indirect allowed transition (plotted as $(\alpha hv)^{1/2}$ versus Eg), n = 3 for an indirect forbidden transition (plotted as $(ahv)^{1/3}$ versus Eg), n = 1/2 for a direct allowed transition (plotted as $(ahv)^2$ versus Eg), n = 3/2 for a direct forbidden transition (plotted as $(ahv)^{2/3}$ versus Eg) [48].

The band gaps of the photocatalyst were then determined by extrapolating the straight line portion of the $(ahv)^2$ versus (hv) graphs to the h *v* axis until $(ah\nu)^{1/n} = 0$. The linear section of these spectra is shown in Fig. 2a and b. The absorption edges of the binary (CdS/CeO_2 and CeO_2/Ag_3PO_4) and ternary [$CdS/CeO_2/Ag_3PO_4$ (1:1, 2:1, 3:1 and 4:1 molar ratio)] photocatalysts are well extended to visible regions of the spectrum compared with the single nanoparticles (Table 1). As can be noted here, formation of ternary systems demonstrated a further red-shift in the visible spectrum which resulted from the interfacial combination and matched band edges between the three semiconductors of the as-synthesized nanocomposites ($CdS/CeO_2/Ag_3PO_4$). The red shift is a result of exhibiting a lower band gap, leading to better visible light harvesting efficiency of the composite favorable for the photocatalytic activity. Based on the band gap results of the ternary systems, $CdS/CeO_2/Ag_3PO_4$ in 4:1 molar ratio (CCA4) was selected for immobilizing onto polyaniline support. The PANI supported ternary system labeled as PAST was also run by UV/Vis to determine its band gap. Its calculated band gap is found to be 2.05 eV. Supporting by polyaniline, in this case, has shifted the absorption band of ternary $CdS/CeO_2/Ag_3PO_4$ (CCA4) nanocomposite further to the visible region making it a better visible active photocatalyst.

Morphology and homogeneity of the as-synthesized photocatalysts: CeO_2, CdS/CeO_2, CeO_2/Ag_3PO_4, $CdS/CeO_2/Ag_3PO_4$ (CCA4) as well as polyaniline supported $CdS/CeO_2/Ag_3PO_4$ (PAST) were investigated by SEM and TEM as shown in Fig. 3. Based on the SEM micrographs shown in Fig. 3a, the morphology of CeO_2 nanoparticle appeared to be nearly cuboidal shape where as the binary (b) and ternary (d) composites exhibited no distinct morphologies. However, cubic like crystals of Ag_3PO_4 appeared sparsely distributed in the sea of CeO_2 nanorods for Ag_3PO_4/CeO_2 system (Fig. 3c). The brightest particles in the PANI supported ternary system observed in Fig. 3e were corroborated as nanoparticles of the heavier metals in particular Ag, Cd and Ce by TEM (Fig. 3f). On the other hand, the estimated percent chemical distribution gradients across the surface of the sample (w/w %) were determined from results of energy dispersive X-ray (EDX) analysis in conjunction with SEM. Interestingly, EDX spectra of all the analyzed samples confirm the presence of Ce, Cd, Ag, S and P (Table 1S). The residual chloride is detected from the HCl used during the *in situ* oxidation of aniline by ammonium persulfate.

The surface functional groups of selected as-synthesized materials, namely, CeO_2, $CdS/CeO_2/Ag_3PO_4$ and $PANI\text{-}CdS/CeO_2/Ag_3PO_4$ were analyzed by FTIR in the range from 400 to 4000 cm^{-1} (Fig. 4 a and b). In the case of CeO_2, the bands at 3435 and 1620 cm^{-1} correspond to the O-H stretching and bending vibration modes respectively, which is originated from physical adsorbed water molecules [49,50]. The band situated around 1047 cm^{-1} has been attributed to the C-O stretching vibration possibly arising from CO_2 absorbed at CeO_2 surface [40]. The wide band positioned at 1315 cm^{-1} consists of the symmetrical stretching mode of N = O and the inside bending mode of N-H. The peak at 850 cm^{-1} may be attributed to outside bending mode of N-H [51,52].

The peaks observed at 1387 cm^{-1} could be ascribed to the stretching vibration of N-O nitrate groups (NO_3-) which resulted from a precursor solution of $Ce(NO_3)_3.6H_2O$ that was used for the synthesis of CeO_2. The intense band at 521 cm^{-1} corresponds to the Ce-O stretching vibration [53]. The FTIR spectral patterns of bare $CdS/CeO_2/Ag_3PO_4$ (CCA4) and PANI supported $CdS/CeO_2/Ag_3PO_4$ (PAST) nanocomposite are depicted in Fig. 4b. Basically, some peaks of both bare and supported photocatalyst exhibited similar patterns except shifts observed by some peaks upon immobilization of the nanocomposite onto the polymer support.

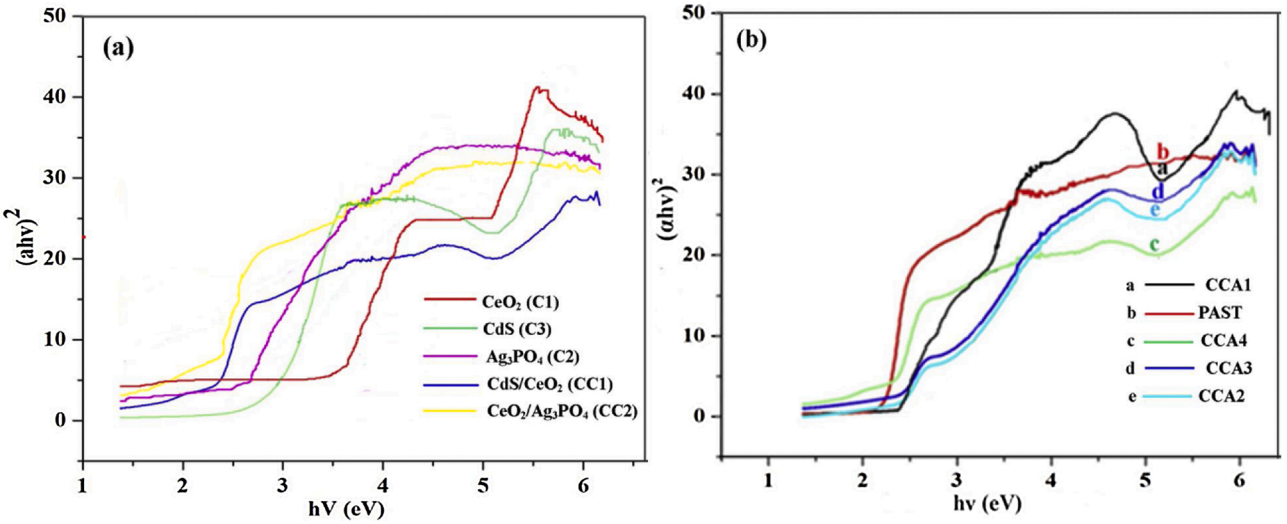

Fig. 2. (a) Tauc plot of single [(CeO_2, Ag_3PO_4 and CdS] and binary [CdS/CeO_2 and CeO_2/Ag_3PO_4] photocatalysts; (b) Tauc plot of bare $CdS/CeO_2/Ag_3PO_4$ (1:1, 2:1, 3:1 and 4:1 molar ratios) and PANI supported ternary nanocomposites.

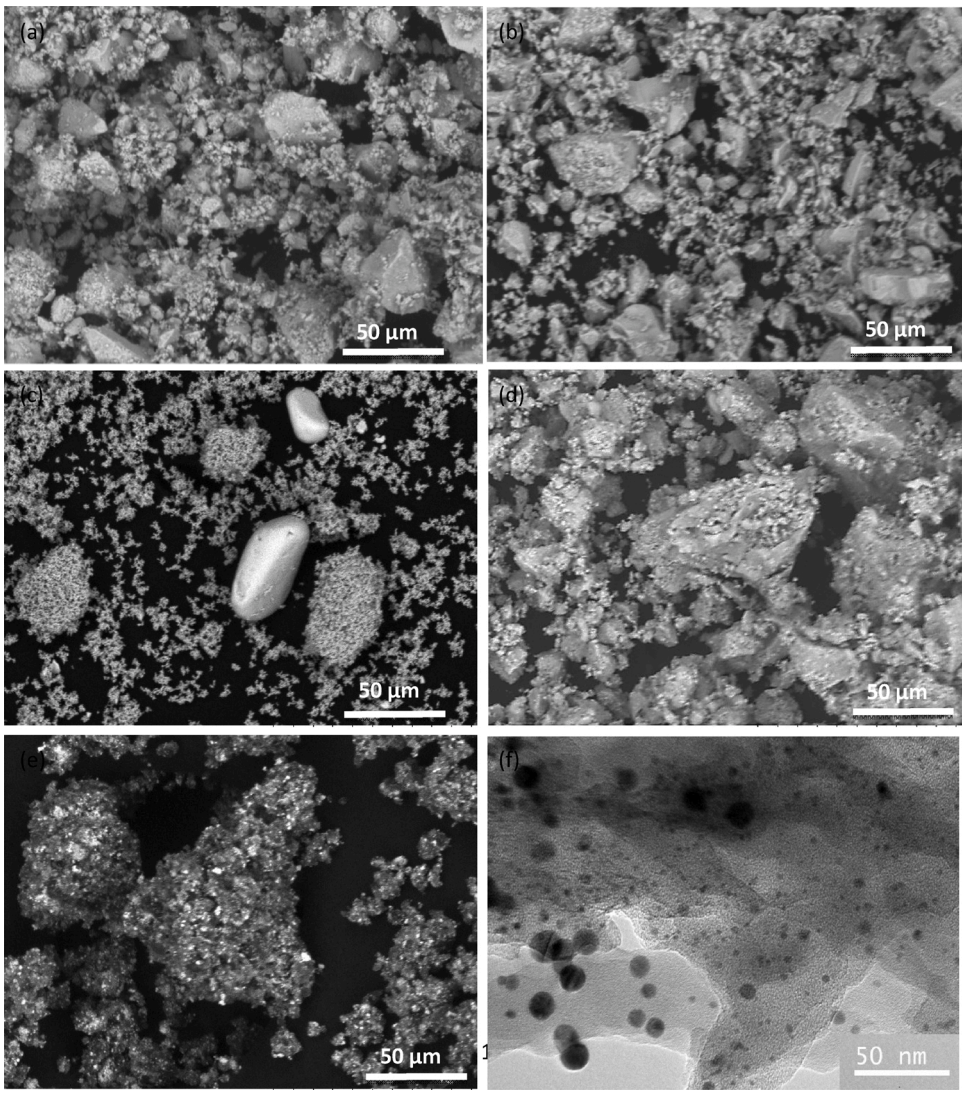

Fig. 3. SEM images of (a) CeO_2, (b) CdS/CeO_2, (c) CeO_2/Ag_3PO_4, (d) $CdS/CeO_2/Ag_3PO_4$ (4:1), (e) Polyaniline supported $CdS/CeO_2/Ag_3PO_4$ photocatalyst and (f) TEM of the later.

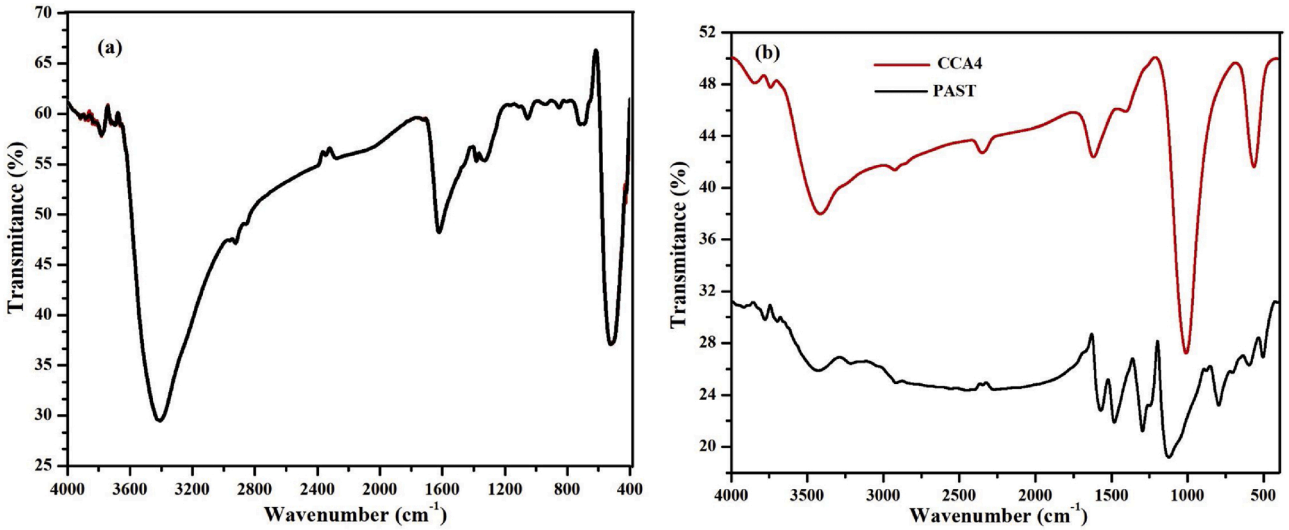

Fig. 4. (a) FTIR spectrum of CeO_2; (b) FTIR spectra of bare $CdS/CeO_2/Ag_3PO_4$ (CCA4) and polyaniline supported $CdS/CeO_2/Ag_3PO_4$ (PAST) nanocomposite.

Accordingly, the bands observed at 3420 (a) and 3410 cm^{-1} (b) are attributed to the presence of O-H stretching vibration that might arise from adsorbed water molecules on the surface of the nanocomposite and may also be due to the action of hydrogen bonding between the hydroxyl groups on the surface CCA4 nanocomposite and the amine groups in the PANI molecular chains [54]. The weak band at 3215 cm^{-1} (supported) could be attributed to the hydrogen bonded N-H stretching vibration between amine and imine sites [55]. The intense band at 1620 (bare) and 1607 (supported) cm^{-1} appeared to be due to -OH (scissor bending) mode of water molecules [49]. In both cases the weak peaks observed around 2920 and 2848 cm^{-1} can be ascribed to asymmetric and symmetric C-H stretching vibrations respectively. And also the strong absorption bands observed around 1007 and 990 cm^{-1} could be attributed to P-O stretching vibrations of phosphate groups (PO_4^{3-}) [56]. The absorption band observed at 545 and 500 cm^{-1} in bare and supported system indicates stretching mode of metal oxide (Ce-O) or sulfide [53].

In the supported composite PAST, the band appeared at 1576 and 1485 cm^{-1} can be attributed to C = C stretching of quinoid diimine unit (the oxidized form of PANI) and C = C aromatic ring stretching of the benzenoid diamine unit (the reduced form of PANI) respectively. The peaks at 1298 and 790 cm^{-1} correspond to C-N stretching vibration mode and N-H out-of-plane deformation vibration mode respectively, which also confirms the formation of PANI in the as-synthesized photocatalyst [57]. In general, the PL intensities of single systems were found to be higher than binary systems and the binary systems intern exhibited higher PL intensities compared to their ternary counterparts (Fig. 5a). In binary and ternary nanocomposites, the photoinduced electrons and holes can be effectively separated and hence excitation PL intensity goes down. This is because, the lower the excitation PL intensity, the stronger the capacity of coupled materials to capture photoinduced electrons, the higher the separation rate of photoinduced electrons and holes, and hence the higher the photocatalytic activity [58]. So, in this study it was clearly observed that the lower PL emission spectra were recorded for CCA4 and PAST (Fig. 5b) justifying the selection of CCA4 for immobilization to the support and employing the same for the subsequent photocatalytic experiment.

4. Photocatalytic studies

4.1. Photocatalytic activity of the as-synthesized materials

In this study, visible light serves as the irradiation source. Methyl orange (MeO), with a characteristic absorption at 464 nm is chosen as a typical model organic pollutant for testing the photocatalytic activity of the as-prepared products. The degradation rate was analyzed by plotting C_t/C_o versus irradiation time (Fig. 6a and b). The photocatalytic activity of single and binary systems are depicted on Fig. 6a whereas bare ternary and supported systems are depicted on Fig. 6b. Before the photocatalytic reaction, an adsorption step in dark conditions was allowed to take place during 60 min to maintain the adsorption/desorption equilibrium. Meanwhile, blank tests were also performed without photocatalyst under the same experimental conditions. It can be seen that after 160 min of visible light irradiation, MeO dye showed negligible degradation (less than 2.8%) without photocatalyst. The photocatalytic activities of pure CeO_2, CdS and Ag_3PO_4 were lower than that of the composite photocatalysts. They decolorized 17.4, 27.7 and 32.1% of MeO in 160 min of irradiation time respectively.

The photocatalytic activity of pure CeO_2 was the lowest among the single systems. The increment of photocatalytic degradation efficiency of CdS and Ag_3PO_4 from that of CeO_2 over MeO solution could be due to the narrow band gap of the formers that make them sensitive to visible portion of the spectrum as evidenced in Table 1 and Fig. 5a. The binary composites CdS/CeO_2 (CC1) and CeO_2/Ag_3PO_4 (CC2) moderately decolorized MeO solution in 160 min of visible light irradiation which is about 38.0 and 43.0% respectively. The increase in degradation efficiency of the binary composites over that of single photocatalysts clearly indicates that the heterojunction or coupling created a condition that favors the enhancement of the degradation efficiency. Among the binary composites, the one comprising CeO_2/Ag_3PO_4 system showed relatively better catalytic activity in contrast to CdS/CeO_2 under visible light irradiation. This variation could be explained in terms of better chance of involving the photogenerated holes (B-Type Heterojunction) in the former case. In A-type heterojunction (CdS/CeO_2), the increased photocatalytic activity of CeO_2 could be initiated by CB electrons of CdS that involve in the photoreduction process. In the band gap configuration of CdS/CeO_2, the electrons generated in CdS transfer from the CB of CdS to that of CeO_2, while the holes remain in the VB of CdS, thus restraining the recombination of electron-hole pairs. Nonetheless, complete oxidation of organic pollutants to CO_2 and H_2O will be slow, due to the unavailability of the •OH radicals on the CeO_2 surface since holes of the CeO_2 have limited involvement [17].

On the other hand, all the ternary CdS/CeO_2/Ag_3PO_4 (1:1, 2:1, 3:1 and 4:1 molar ratios) composites exhibit the highest photocatalytic activity compared with their single (CeO_2, CdS and Ag_3PO_4) and binary

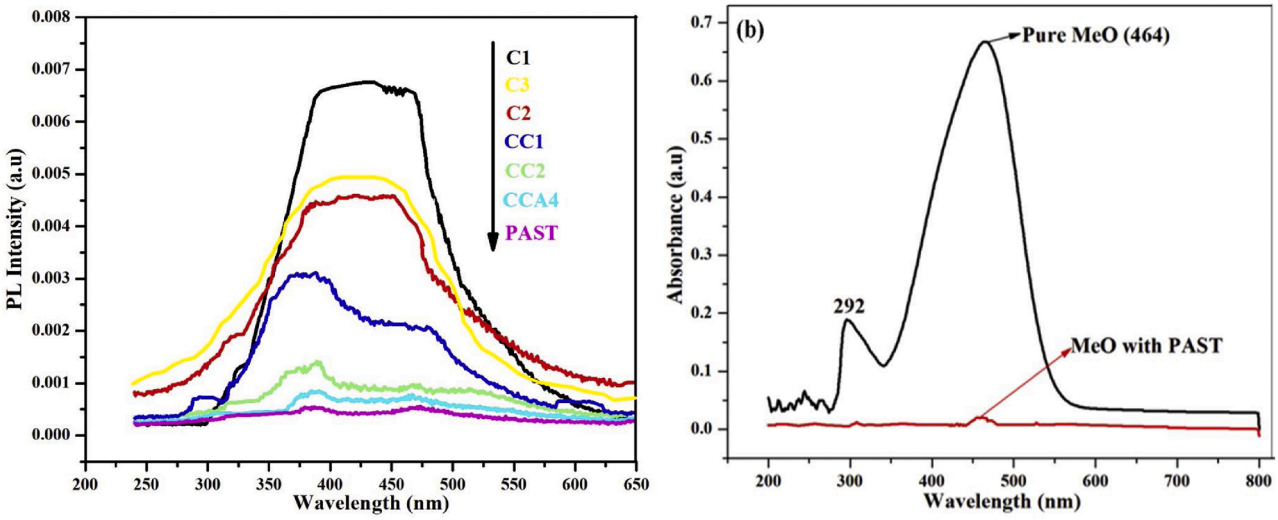

Fig. 5. (a) The PL emission spectra of CeO_2 (C1), CdS (C3), Ag_3PO_4 (C2), CdS/CeO_2 (CC1), CeO_2/Ag_3PO_4 (CC2), CdS/CeO_2/Ag_3PO_4 (CCA4) and polyaniline supported CdS/CeO_2/Ag_3PO_4 (PAST) photocatalysts; (b) UV/Visible absorption spectra of methyl orange with and without PAST photocatalyst (after 160 min of irradiation time).

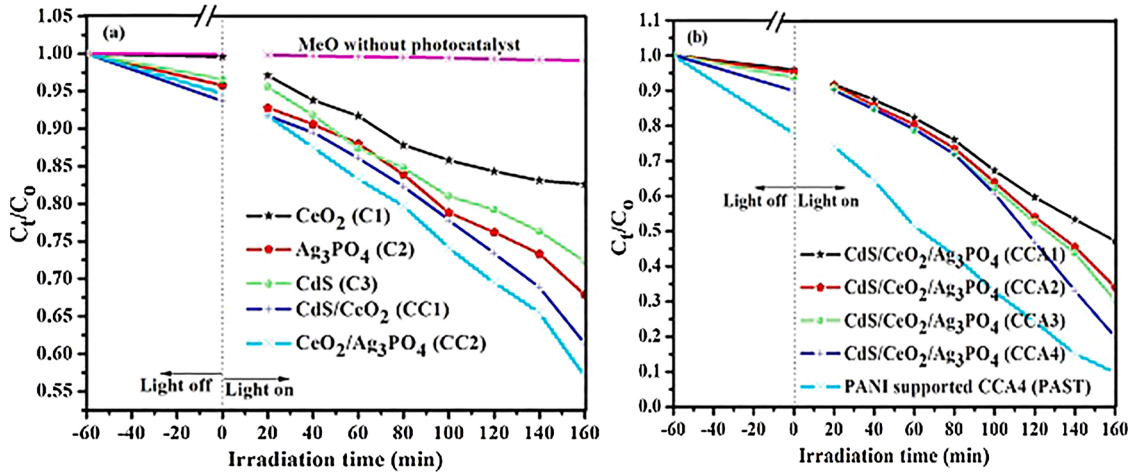

Fig. 6. (a). Degradation efficiency of the as-synthesized photocatalyst [CeO_2 (C1), Ag_3PO_4 (C2), CdS (C3), CdS/CeO_2 (CC1) and CeO_2/Ag_3PO_4 (CC2)] as function of visible irradiation time ; (b) Photocatalytic degradation of the as-synthesized bare ternary (CCA1, CCA2, CCA3 and CCA4) and supported nanocomposite (PAST) as function of time under visible irradiation.

(CdS/CeO_2 and CeO_2/Ag_3PO_4) congeners. The reason for the enhancement in the photocatalytic activity of the ternary nanocomposite is that having more than one path for the formation of electron-hole pair because of the three different interfaces and the delayed electron-hole pair recombination as confirmed by the PL results [59]. Among the four tested ternary systems, CCA4 with 4:1 molar ratio of CdS to CeO_2/Ag_3PO_4 (CCA4) have exhibited the highest photocatalytic activity. The enhancement is due to the effective loading of CdS on CeO_2/Ag_3PO_4 nanocomposite to create visible sensitive heterojunction increasing its photoabsorption capacity in visible region and prolonged electron hole recombination as witnessed in Table 1 and Fig. 5a. The photocatalyst comprising polyaniline supported CdS/CeO_2/Ag_3PO_4 (PAST) exhibited much higher percentage degradation (90.22%) compared to naked ternary counterparts (Fig. 6b). This could be due to efficient charge separation of e- and h^+ pairs in the excited states that prevents recombination of charge pairs for a longer time under visible irradiation. Also, the conducting polymer PANI has an extended π -conjugated electron system with narrow band gap and high absorption coefficients in the visible light range, serving it as an excellent electron donor and a good hole acceptor when illuminated [60] rendering the hybrid nanocomposite (PAST) highly efficient.

4.2. *Effect of operational parameters*

4.2.1. *Effect of pH*

Point of zero harge (PZC) for a given catalyst surface is the pH at which that surface has zero or a net neutral charge. We estimated the pHpzc value of the supported photocatalyst (PAST) and found an approximate value of 5.1(Fig. 7a). Accordingly, the photocatalyst surface prones to be acidic at pH below 5.1, basic at pH above 5.1 and neutral at pH = 5.1. This parameter is important as the interaction between the photocatalyst and target pollutant dye is contingent up on it. The pH is one of an important parameter of adsorption process as it affects the surface charge of the adsorbent, degree of ionization of target pollutants and dissociation of functional groups on the active site of adsorbent [61]. The degradation of MeO solution at initial concentration (10 ppm) and photocatalyst load (0.2 g/L) as a function of irradiation time is shown in Fig. 7b. The photodegradation result (Fig. 7b) revealed that higher adsorption and higher photocatalysis was obtained at pH 4.0 which is less than the pH_{PZC} of the catalyst. This is due to the higher interaction between the positively charged surface of the photocatalyst particles and the anionic dye methyl orange (MeO) at this pH. The photocatalytic degradation of MeO by PAST increased from 75.0 to 91.5% between pH 2 and pH 4 but decreased from 91.5 to 54.5% as pH

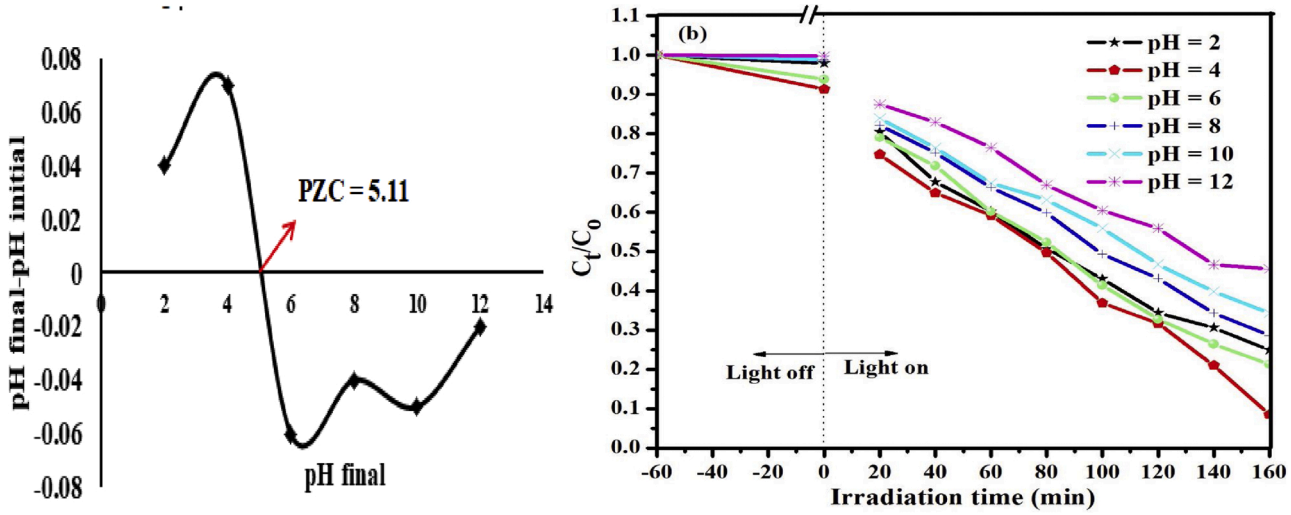

Fig. 7. (a) Plot of point of zero charge of the PANI supported CdS/CeO_2/Ag_3PO_4 photocatalyst; (b) Effect of initial pH of the dye on the degradation of MeO as a function of irradiation time (PAST load at 0.2 g/L and initial concentration of MeO at 10 ppm).

enhanced to 12 in 160 min irradiation time. The degradation rate constant (k) was found to be 0.0154, 0.0097, 0.0087, 0.0079, 0.0067 and 0.0049 min^{-1} at solution pH 4, 6, 2, 8, 10 and 12 respectively. It is concluded that the degradation rate decreased with increasing basicity, which may be explained by the ionization state of PAST nanoparticle and the existence of the sulphonate group (SO^{-3}) of the anionic MeO dye which favored electrostatic repulsion. At pH4, PAST is positively charged, while MeO is negatively charged which means that strong electrostatic interaction is resulted favoring strong adsorption of MeO molecules which makes them close to the center of the electron-hole pair generation and their subsequent degradation [43,61].

4.2.2. Effect of initial concentration of MeO

Another important factor in photocatalytic degradation study is the initial concentration of the organic pollutant (MeO). Effect of the initial concentration of MeO solution on the degradation effect under visible irradiation utilizing PANI supported $CdS/CeO_2/Ag_3PO_4$ (PAST) was studied by varying the concentrations from 10 to 35 ppm at fixed pH (4) and photocatalyst load (0.2 g/L). The degradation rate of PAST showed reciprocal relationship with dye initial concentration (10, 15, 20, 25 and 35 ppm). It is found that 91.4% of the dye was removed after 160 min when the dye concentration was 10 ppm and the decomposition decreased to 37.1% when the concentration increased to 35 ppm (Fig. 8a). The corresponding degradation rate constant (k) also decreased in the order 0.0154, 0.0105, 0.0070, 0.0055 and 0.0029 min^{-1} at 160 min of irradiation time respectively. The decrease in the degradation of MeO as the concentration increased can be attributed to two factors. The first may be because of the limited number of active sites available when compared with the number of MeO molecules present at higher concentrations. At higher MeO concentrations, the active sites may be covered by the excess of MeO molecules, hindering the effectiveness of the catalyst. The second factor can be due to a shielding effect. This prevents the interactions of photons of the light with the system, thus resulting to decreased photodegradation efficiency [62].

4.2.3. Effect of photocatalyst load

The effect of photocatalyst amount on the rate of degradation of MeO was carried out by using different amounts of PANI supported $CdS/CeO_2/Ag_3PO_4$ (PAST) nanocomposite in the range of 0.05-0.4 g/L. As shown in the Fig. 8b, degradation rate increases with increasing catalyst load from 0.05 to 0.15 g/L; further increases of catalyst amount from 0.15 g/L to 0.4 g/L however resulted in decreased degradation of MeO. The rate of degradation of MeO rose remarkably from 49.1 to 93.9% with the rise of photocatalyst dosage and fall of from 69.7% when the dosage becomes bulky. The corresponding rate constant (k) for 0.05, 0.1, 0.15, 0.3 and 0.4 g/L load were 0.0040, 0.0074, 0.0176, 0.0096 and 0.0055 min^{-1} at 160 min irradiation time respectively. The increased degradation rate with load could be due to greater number of exchangeable sites available for interaction with dye molecules [61]. The increase of adsorbent dosage also contributes to the increase of surface area (for a given reactor design) along with increased active functional group available on the adsorption site. However, the increase in the amount of catalyst has caused a negative effect beyond a certain optimum. This is due to the fact that when the concentration of the catalyst rises, the solid particles increasingly block the penetration of the radiation. Hence, the overall number of the photons reaching to the catalyst active sites and the production of active radicals decreases [62].

4.2.4. Effect of scavengers

It is known that the principal factor of photocatalysis is the generation of reactive radicals. Therefore, it is necessary to evaluate the nature of the reactive radicals responsible for the catalytic degradation. In this work, $NaHCO_3$ (h^+ scavenger), $AgNO_3$ ($\bullet O_2$- scavenger) and methanol ($\bullet$OH scavenger) [63] were used to scavenge the reactive species. Fig. 9a shows the photodegradation of MeO in the presence and absence of the scavengers. The photocatalytic degradation of MeO is 91.8% in the absence of the scavengers. The degradation efficiency decreased to 82.8, 70.6 and 61.1% when $NaHCO_3$, CH_3OH and $AgNO_3$ were added as scavengers. The results indicated that all the scavengers considered have suppressed the photocatalytic degradation efficiency although the effect of $AgNO_3$ and CH_3OH are more pronounced. The addition of $NaHCO_3$ slightly changed the photocatalytic degradation of the target dye. Therefore, the main active species in this photodegradation reaction is superoxide and hydroxyl radicals. The decrease of the removal rate in the presence of scavengers presents the following trend: $AgNO_3 > CH_3OH > NaHCO_3$. The direct involvement of holes appeared to be restricted. Rather the holes involve indirectly via the reaction of these species with water molecules to create a very reactive hydroxyl radicals. This experiment evidences the involvement of the conduction band electrons and the valence band holes in the redox process corroborating the highest photocatalytic efficiency of the ternary systems compared to their binary congeners.

4.3. Recyclability

In addition to photocatalytic efficiency, the recyclability of a

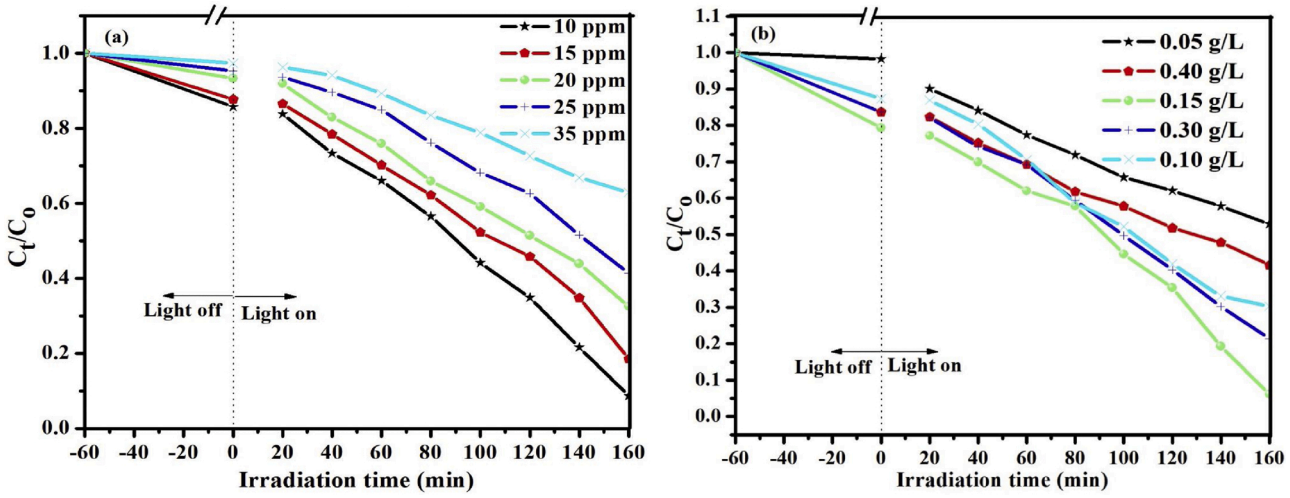

Fig. 8. (a). Effect of initial dye concentration on the degradation rate of MeO as function of irradiation time (PAST load at 0.2 g/L, initial concentration of MeO at10 ppm and pH at 4); (b) The effect of PAST photocatalyst load on MeO dye degradation as a function of irradiation time (initial concentration of MeO at 10 ppm and pH at 4).

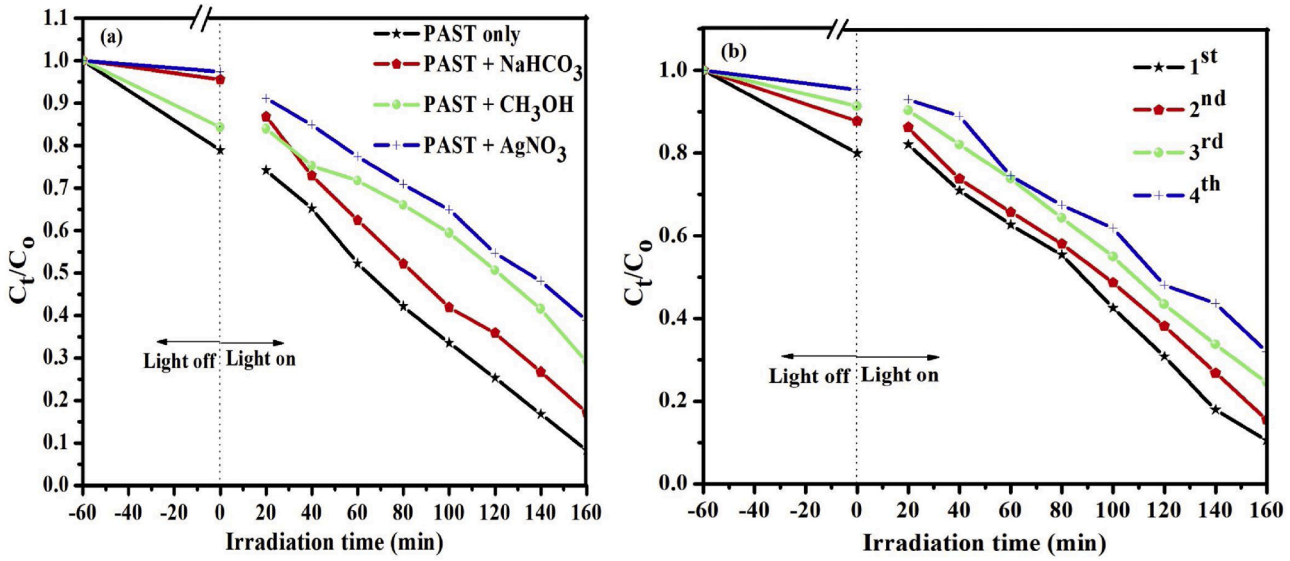

Fig. 9. (a). Degradation rate of MeO as function of irradiation time in the absence and presence of scavengers (PAST load at 0.15 g/L, initial concentration of MeO at 10 ppm and pH at 4); (b) Degradation rate of MeO using PAST photocatalyst as function of irradiation time in different cycles (PAST load at 0.15 g/L, initial concentration of MeO at 10 ppm and pH at 4).

photocatalyst is also very important for practical application. To evaluate the reusability of PAST, the circulating run in the photocatalytic degradation of MeO was carried out under visible light irradiation. The process was repeated up to four times. As shown in Fig. 9b, the first cycle degraded 89.52% of the dye after 160 min of irradiation time. Subsequently the second, third and fourth cycles degraded 84.53, 75.49 and 68.06% of the dye corresponding to the rate constant (k) 0.0141 to 0.0117, 0.0088 and 0.0071 min^{-1} respectively. Agglomeration and sedimentation of the dye around PAST particles after each cycle of photocatalytic degradation is a possible cause of the observed decrease on the degradation rate, because each time the photocatalyst is reused new parts of the photocatalyst surface become unavailable for dye adsorption and thus photon absorption, reducing the efficiency of the catalytic reaction. In addition to this, loss of some catalyst during the recycling process is a possibility in regenerating the photocatalyst material accounting for the decline of photodegraradtion efficiency. Despite this, PAST demonstrated good stability after recovery and that catalyst reuse is effective. The result demonstrates that PANI supported $CdS/CeO_2/Ag_3PO_4$ nanocomposite shows excellent photocatalytic performance in addition to a fairly good stability after 4 cycles in 160 min.

4.4. Decolorization of real sample

The efficiency of the as-synthesized PANI supported $CdS/CeO_2/Ag_3PO_4$ (PAST) photocatalyst for the degradation of the real sample under visible light irradiation was studied under 160 min visible light irradiation. This experiment was undertaken based on the optimum values set for degradation of the model pollutant just to observe the performance of the photocatalytic material. As the result, we haven't undergone any physicochemical analysis on the same. Fig. 10a showed the percentage degradation of the model pollutant (MeO) and the real sample textile effluent collected from Bahir Dar. The efficiency was found to be 93.4 and 70.7% with k value of 0.0167 and 0.0079 min^{-1} respectively. The degradation efficiency of the real sample was reduced compared to the optimized one, the model pollutant (MeO). Extrapolation of any mechanism for the observed fact is rather difficult in this

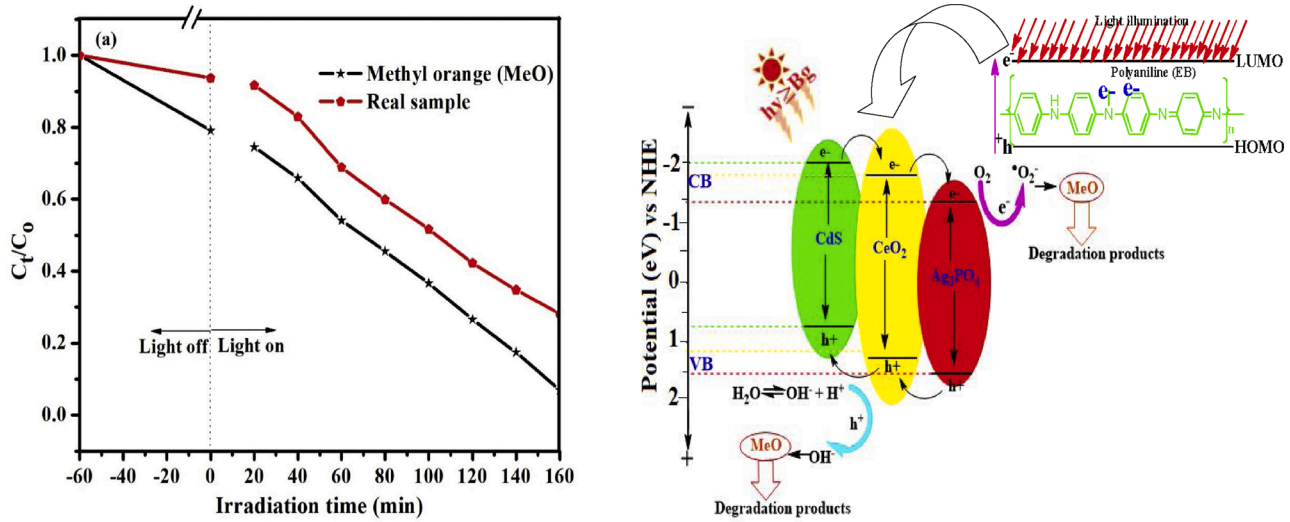

Fig. 10. (a). Degradation of real and model sample (MeO) using PAST photocatalyst as a function of irradiation time (PAST load at 0.15 g/L, initial concentration of MeO at 10 ppm and pH at 4); (b). Mechanism of photocatalytic degradation of organic contaminant (MeO) by PAST photocatalyst under visible light irradiation.

case due to the complexity of the wastewater which includes not only mixture of organic dyes but also other chemicals from the bleaching steps [23,42].

4.5. Proposed mechanism of degradation

Photocatalytic degradation mechanism of methyl orange dye over PANI supported $CdS/CeO_2/Ag_3PO_4$ ternary composite is proposed as illustrated in Fig. 10b. CdS, CeO_2 and Ag_3PO_4 are n-type semiconductors. Compositing these semiconductors with each other results to n-n-n ternary heterojunctions [64,65] among CdS, CeO_2 and Ag_3PO_4. The separation of photogenerated species could be better apprehended by calculating the flat band potentials and estimating the band gap energies of the semiconductors involved. To this effect, we calculated the conduction band (CB) and valence band (VB) energies of CdS, CeO_2, and Ag_3PO_4 semiconductors using the following empirical equations: $E_{CB} = X - E_c - 0.5E_g$ and $E_{VB} = E_{CB} + E_g$ where X is the absolute electronegativity of the semiconductor; E_C, E_{cB}, E_{VB}, and E_g are the energy of free electrons on the hydrogen scale (4.5 eV), conduction band energy, valence band energy and the band gap energy of the semiconductor, respectively [36].

According to the above equations, E_{VB} and E_{CB} values of CdS, CeO_2, and Ag_3PO_4 were calculated to be 1.02, 2.70, 2.89 and -1.46, -0.56, 0.52 eV respectively. A band edge position of these semiconductors is schematically illustrated in Fig. 10b. Since the CB of CeO_2 is placed lower than that of CdS and higher than that of Ag_3PO_4, the $CdS/CeO_2/Ag_3PO_4$ hetrojunction would operate effectively owing to the established cascade structure of the CB positions in the hybrid. In this group, difference between the energy levels for the CB of the combined semiconductors forces a quick transfer of the photoexcited electrons from one semiconductor to another adjacent semiconductors in cascade form, thus enhancing the separation of e/h + pairs and hence the photocatalytic efficacy [20]. In such ternary systems, formation of "A-B Type" tandem n-n hetrojunctions is possible. As the result, the photoinduced electrons and holes are efficiently separated from each other and their recombination prolonged, which is consistent with the PL results. Consequently, the ternary composite exhibited highly enhanced photocatalytic activity compared with its single and binary counterparts. Moreover, it is well known that in photocatalytic processes, a series of reactive species such as hydroxyl radical (•OH), active holes (h^+), and superoxide ion radicals ($\bullet O_2$-) are generated after production of electrons and holes. In order to evaluate the roles of these species, different scavengers were employed and added to the reaction system during the degradation reaction. In our case, we employed different scavengers such as $AgNO_3$ for superoxide radical ($\bullet O_2$-), $NaHCO_3$ for h^+, and CH_3OH for •OH [13]. As can be seen from Fig. 6b, the photodegradation of MO was inhibited by the addition of scavengers to a various extent. The photocatalytic degradation of MO is recorded to be 91.8% in the absence of scavengers. However, the presence of the scavengers $AgNO_3$, $NaHCO_3$ and CH_3OH showed a respective 31, 9, and 21% reduction in the degradation of MO dye. This result shows the involvement of all the three species in the degradation processes although significant contribution is made by superoxide and hydroxyl radicals. The result obtained from trapping experiment confirms the mechanism proposed in Fig. 10b. The superior photocatalytic activity of PAST compared with binary and bare ternary rivals might have resulted from the enhanced charge separation and the formation of more active radicals ($\bullet O_2$- and •OH) which are induced by the synergetic effect between PANI and CCA4. It is noteworthy that the conducting PANI on the surface of CCA4 could absorb photons in the visible light which leads to an efficient photogenerated e–h^+ pairs. Also the conducting polymer PANI with narrow band gap and high absorption coefficients in the visible light range renders it act as an excellent electron donor and a good hole acceptor when illuminated [59,60] making PAST highly efficient.

5. Conclusion

In this study, single (CdS, CeO_2 and Ag_3PO_4) nanoparticles, and binary (CdS/CeO_2 and CeO_2/Ag_3PO_4) and ternary ($CdS/CeO_2/Ag_3PO_4$ in different molar ratios) composites were synthesized via precipitation method. Polyaniline supported $CdS/CeO_2/Ag_3PO_4$ nanocomposite was also synthesized by "*in situ*" chemical oxidative polymerization method. Crystal structure, surface area, morphology, band gap energy, functional groups (bond vibration; stretching as well as bending) and optical properties of the as-synthesized photocatalysts confirmed the formation of an "A-B" type tandem n-n heterojunction composite with a band gap sensitive to visible irradiation. Photocatalytic activities of as-obtained photocatalysts were investigated for the degradation of MeO dye under visible light irradiation. Results showed highest photocatalytic activity achieved by PAST compared with its single, binary and unsupported ternary counterparts. It has been found that operating parameters such as solution pH, initial dye concentration, photocatalyst load and the existence of different scavengers had their influences on the degradation of methyl orange (MeO). The results confirmed the following optimum values: pH 4, initial dye concentration 10 ppm and photocatalyst load 0.15 g/L. The effects of different scavengers suggest that $\bullet O_2$- and •OH scavengers play major roles in the degradation of MeO. Furthermore, stability test has shown that the photocatalytic activity of PAST was reasonably good after four reaction recycles. The photocatalytic nanocomposite (PAST) has also demonstrated fairly high degradation efficieny (70.4%) on the textile effluent collected from one of the local textile factory in Bahir Dar, Ethiopia, revealing its potential application for dye effluent treatment.

CRediT authorship contribution statement

Abi M. Taddesse: Conceptualization, Methodology, Writing - review & editing, Supervision. **Tigabu Bekele:** Methodology, Data curation, Software, Writing - original draft. **Isabel Diaz:** Supervision, Software, Writing - review & editing. **Abebaw Adgo:** Supervision, Writing - review & editing.

Declaration of Competing Interest

This manuscript entitled "Polyaniline supported $CdS/CeO_2/Ag_3PO_4$ nanocomposite: An "A-B" type tandem n-n heterojunctions with enhanced photocatalytic activity" consists of a table and 10 figures. It has not been published previously (except in the form of an academic thesis in Haramaya University); it is not under consideration for publication elsewhere. The manuscript is sent up on the approval of all authors. If accepted, it will not be published elsewhere in the same form, in English or in any other language, including electronically without the written consent of the copyright-holder.

Acknowledgements

Abi M. Taddesse would like to acknowledge the research grant received from Ministry of Education through office of the Research and Extension, Haramaya University (HURG-2016-03-02). I. D. acknowledges the funding from the Spanish Research Agency (AEI) and the European Regional Development Fund (FEDER) through the Project MAT2016-77496-R (AEI/FEDER, UE).

References

[1] S. Benkhaya, S. M'rabet, A. El Harfi, Classifications, properties, recent synthesis and applications of azo dyes Heliyon 6, 2020 e03271.
[2] S. Benkhaya, S. Mrabet, A. El Harfi, A review on classifications, recent Synthesis and applications of textile dyes Inorg. Chem. Commun. DOI: https://doi.org/10.1016/j.inoche.2020.107891.
[3] B.C. Ventura-Camargo, M.A. Marin-Morales, Azo dyes: Characterization and toxicity– A review, Text. Light Ind. Sci. Techn. (TLIST) 2 (2013) 85–103.

[4] M.A. Semião, C.W.I. Haminiuk, G.M. Maciel, Residual diatomaceous earth as a potential and cost effective biosorbent of the azo textile dye Reactive Blue 160, J. Environ. Chem. Eng. 8 (2020), 103617.
[5] Y. Zhou, J. Lu, Y. Zhou, Y. Liu, Recent advances for dyes removal using novel adsorbents: A review, Env. Poll. 252 (2019) 352–365.
[6] V. Katheresan, J. Kansedo, S.Y. Lau, Efficiency of various recent wastewater dye removal methods: A review, J. Environ. Chem. Eng. 6 (2018) 4676–4697.
[7] L.V. Bora, R.K. Mewada, Visible/solar light active photocatalysts for organic effluent treatment: Fundamentals, mechanisms and parametric review, Renew. Sust. Energ. Rev. 76 (2017) 1393–1421.
[8] W. Xiong, W. Dai, X. Hu, L. Yang, T. Wang, Y. Qin, X. Luo, J. Zou, Enhanced photocatalytic reduction of CO2 into alcohols on Z-scheme Ag/Ag3PO4/CeO2 driven by visible light, Mater. Lett. 232 (2018) 36–39.
[9] N. Wetchakun, S. Chaiwichain, K. Wetchakun, W. Kangwansupamonkonc, B. Inceesungvorn, S. Phanichphant, Synthesis and characterization of novel magnetically separable CoFe2O4/CeO2 nanocomposite photocatalysts, Mater. Lett. 113 (2013) 76–79.
[10] R. Ma, S. Zhang, T. Wen, P. Gu, L. Li, G. Zhao, F. Niu, Q. Huang, Z. Tang, X. Wang, A critical review on visible-light-response CeO2-based photocatalysts with enhanced photooxidation of organic pollutants, Catal. Today 335 (2019) 20–30.
[11] A.A. Ali, A.A. Nazeer, M. Madkour, A. Bumajdad, F. Al Sagheer, Novel supercapacitor electrodes based semiconductor nanoheterostructure of CdS/rGO/CeO2 as efficient candidates, Arab. J. Chem. 11 (2018) 692–699.
[12] Z.M. Yang, G.F. Huang, W.Q. Huang, J.M. Wei, X.G. Yan, Y.Y. Liu, C. Jiao, Z. Wan, A. Pan, Novel Ag3PO4/CeO2 composite with high efficiency and stability for photocatalytic applications, J. Mater. Chem. A. 2 (2014) 1750–1756.
[13] J. Chaison, K. Wetchakun, N. Wetchakun, Investigation of the physical, optical, and photocatalytic properties of CeO2/Fe-doped InVO4 composite, J. Phys. Chem. Solids 111 (2017) 95–103.
[14] M.K. Kesarla, M.O. Fuentez-Torres, M.A. Alcudia-Ramosb, F. Ortiz-Chi, C. G. Espinosa-González, M. Alemand, J.G. Torres-Torres, S. Godavarthi, Synthesis of g-C3N4/N-doped CeO2composite for photocatalytic degradation of an herbicide, J. Mater. Res. Technol. (2018), https://doi.org/10.1016/j.jmrt.2018.11.008.
[15] S. Ijaz, M.F. Ehsan, M.N. Ashiq, N. Karamat, T. He, Preparation of CdS@CeO2 core/shell composite for photocatalytic reduction of CO2 under visible-light irradiation, Appl. Surf. Sci. 390 (2016) 550–559.
[16] D. You, B. Pan, F. Jiang, Y. Zhou, W. Su, CdS nanoparticles/CeO2 nanorods composite with high-efficiency visible-light-driven photocatalytic activity, Appl. Surf. Sci. 363 (2016) 154–160.
[17] W. Liu, M. Wanga, C. Xu, S. Chen, X. Fu, Ag3PO4/ZnO: An efficient visible-light-sensitized composite with its application in photocatalytic degradation of Rhodamine B, Mater. Res. Bull. 48 (2013) 106–113.
[18] S.B. Rawal, S.D. Sung, W.I. Lee, Novel Ag3PO4/TiO2 composites for efficient decomposition of gaseous 2-propanol under visible-light irradiation, Catal. Commun. 17 (2012) 131–135.
[19] W. Lin, S. Zhang, D. Wan, C. Zhang, D. Sun, Ultrasound-assisted synthesis of high-efficiency Ag3PO4/CeO2 heterojunction photocatalyst, Ceram. Intern. 41 (2015) 8956–8963.
[20] T. Montini, M. Melchionna, M. Monai, P. Fornasiero, Fundamentals and catalytic applications of CeO2-based materials, Chem. Rev. 116 (2016) 5987–6041.
[21] M. Pirhashemi, A. Habibi-Yangjeh, S.R. Pouran, Review on the criteria anticipated for the fabrication of highly efficient ZnO-based visible-light-driven photocatalysts, J. Ind. Eng. Chem. 62 (2018) 1–25.
[22] J. Li, Z. Liu, Z. Zhu, Enhanced photocatalytic activity in ZnFe2O4–ZnO–Ag3PO4 hollow nanospheres through the cascadal electron transfer with magnetical separation, J. Alloy. Compd. 636 (2015) 229–233.
[23] X. Rong, F. Qiu, Z. Jiang, J. Rong, J. Pan, T. Zhang, D. Yang, Preparation of ternary combined ZnO-Ag2O/porous g-C3N4composite photocatalyst and enhanced visible-light photocatalytic activity for degradation of ciprofloxacin, Chem. Eng. Res. Des. 111 (2016) 253.
[24] Z. Jingchang, G. Lingling, C. Weiliang, Synthesis of Ti-Ce-Si binary and ternary nanocomposite phatocatalyst by supercritical fluid drying technology, J. Rare Earth. 24 (2006) 182–187.
[25] A. Ameen, M.S. Akhtar, Y.S. Kim, B. Yang, H.S. Shin, An effective nanocomposite of polyaniline and ZnO: Preparation, characterizations, and its photocatalytic activity, Colloid Polym. Sci. 289 (2011) 415–421.
[26] Y. Bu, Z. Chen, Role of polyaniline on the photocatalytic degradation and stability performance of the Polyaniline/Silver/Silver Phosphate composite under visible light, ACS Appl. Mater. Interfaces 6 (2014) 17589–17598.
[27] D. Hidalgo, S. Bocchini, M. Fontana, G. Saraccob, S. Hernandez, Green and low-cost synthesis of PANI-TiO2 nanocomposite mesoporous films for photoelectrochemical water splitting, RSC Adv. 5 (2015) 49429–49438.
[28] P. Latha, K. Prakash, S. Karuthapandian, Enhanced visible light photocatalytic activity of CeO2/alumina nanocomposite: Synthesized via facile mixing-calcination method for dye degradation, Adv. Powder Technol. 28 (2017) 2903–2913.
[29] Y. Bi, S. Ouyang, J. Cao, J. Ye, Facile synthesis of rhombic dodecahedra AgX/Ag3PO4 (X = Cl, Br, I) hetrocrystals with enhanced photocatalytic properties and stabilities, J. Phys. Chem. 13 (2011) 10071–10075.
[30] V. Singh, P. Sharma, P. Chauhan, Synthesis of CdS nanoparticles with enhanced optical properties, Mater. Charact. 62 (2011) 43–52.
[31] S. Ijaz, M.F. Ehsan, M.N. Ashiq, N. Karamat, T. He, Preparation of CdS/CeO2 core/shell composite for photocatalytic reduction of CO2 under visible-light irradiation, Appl. Surf. Sci. 390 (2016) 550–559.
[32] Y. Song, H. Zhao, Z. Chen, W. Wang, L. Huang, H. Xu, H. Li, The CeO2/Ag3PO4 photocatalyst with stability and high photocatalytic activity under visible light irradiation, Phys. Status Solidi A 213 (2016) 2356–2363.
[33] M. Anjum, M. Oves, R. Kumar, M.A. Barakat, Fabrication of ZnO-ZnS/polyaniline for photocatalytic degradation of 2-chlorophenol and microbial contaminants in wastewater, Int. Biodeter. 119 (2017) 66–77.
[34] B. Semagne, I. Diaz, T. Kebede, Abi M. Taddesse, Synthesis, characterization and analytical application of Polyaniline tin (IV) molybdophosphate composite with nanocrystalline domains, React. Funct. Polym. 98 (2016) (2016) 17–23.
[35] R.Y. Hong, J.H. Li, L.L. Chen, D.Q. Liu, H.Z. Li, Y. Zheng, J. Ding, Synthesis, surface modification and photocatalytic property of ZnO nanoparticles, Powder Techno. 189 (2009) 426–432.
[36] S. Kaur, V. Singh, TiO2 mediated photocatalytic degradation studies of Reactive Red by UV irradiation, J. Hazard. Mater. 141 (2007) 230–236.
[37] B. Liu, X. Zhao, C. Terashima, A. Fujishima, K. Nakata, Thermodynamic and kinetic analysis of heterogeneous photocatalysis for semiconductor systems, Phys. Chem. Chem. Phys. 16 (2014) 8751–8760.
[38] S. Panumati, K. Chudecha, P. Vankhaew, Adsorption of phenol from diluted aqueous solutions by activated carbons obtained from bagasse, oil palm shell and pericarp of rubber fruit, J. Sci. Technol. 30 (2008) 185–189.
[39] J. Roggenbuck, H. Schaer, T. Tsoncheva, C. Minchev, J. Hanss, M. Tiemann, Mesoporous CeO2: Synthesis by nanocasting, characterization and catalytic properties, Micropor. Mesopor. Mat. 101 (2007) 335–341.
[40] B. Liu, Z. Li, S. Xu, D. Han, D. Lu, Enhanced visible-light photocatalytic activities of Ag3PO4/MWCNT nanocomposite fabricated by facile in situ precipitation method, J. Alloy. Compd. 596 (2014) 19–24.
[41] X. Zhang, N. Zhang, Y. Xu, Z.R. Tang, One-dimensional CdS-CeO2 composites with boosted photocatalytic activity, New J. Chem. 39 (2015) 6756–6764.
[42] D. You, B. Pan, Y. F.Jiang, W. Zhou, Su, CdS nanoparticle/CeO2 nanorods composite with high efficiency visible light driven photocatalytic activity, Appl. Surf. Sci. 363 (2016) 154–160.
[43] A. Ameen, M.S. Akhtar, S.G. Ansari, O.B. Yang, H.S. Shin, Electrophoretically deposited polyaniline/ZnO nanoparticles for pen heterostructure diodes, Superlattices Microst. 46 (2009) 872–880.
[44] U.I. Gaya, Heterogeneous photocatalysis using inorganic semiconductor solids, Springer, Dordrecht Heidelberg, London, New York, 2014. PP 222.
[45] M.N. Chonga, B. Jin, W.K. Christopher Chow, C. Saint, Recent developments in photocatalytic water treatment technology: A review, Water Res. 44 (2010) 2997–3027.
[46] P. Kubelka, F. Munk, Use of diffuse reflectance spectroscopy for optical characterization of un-supported nanostructures, J. Appl. Phys. 12 (1931) 593–620.
[47] T. Tauc, F. Abeies, Optical properties of solids, IOP Publishing Ltd, North Holland, Amsterdam, 1970. PP 903.
[48] R. Lopez, R. Gomez, Band-gap energy estimation from diffuse reflectance measurements on sol-gel and commercial TiO2: A comparative study, J. Sol-Gel Sci. Techn. 61 (2012) 1–7.
[49] M. Zawadzki, Preparation and characterization of ceria nanoparticles by microwave-assisted solvothermal process, J. Alloy Compd. 454 (2008) 347–351.
[50] M.L. Dos Santos, R.C. Lima, C.S. Riccardi, R.L. Tranquilin, P.R. Bueno, J.A. Varela, E. Longo, Preparation and characterization of ceria nanospheres by microwave-hydrothermal method, Mater. Lett. 62 (2008) 4509–4511.
[51] M. Prekajski, V. Fruth, C. Andronescu, L.V. Trandafilovic, J. Pantic, A. Kremenovic, B. Matovic, Thermal stability of Ce1-xBixO2-δ (x = 0.1-0.5) solid solution, J. Alloy. Compd. 578 (2013) 26–31.
[52] X. Yu, P. Ye, L. Yang, S. Yang, P. Zhou, W. Gao, Preparation of hexagonal cerium oxide nanoflakes by a surfactant free route and its optical property, J. Mat. Res. 22 (2007) 3006–3013.
[53] C. Ho, J.C. Yu, T. Kwong, A.C. Mak, S. Lai, Morphology controllable synthesis of mesoporous CeO2 nano and microstructures, Chem. Mater. 17 (2005) 4514–4522.
[54] Y. He, Preparation of polyaniline/nano-ZnO composites via a novel, Pickering emulsion route, Powder Technol. 147 (2004) 59–63.
[55] S. Sarmah, A. Kumar, Photocatalytic activity of polyaniline-TiO2 nanocomposite, Indian J. Phys. 85 (2011) 713–726.
[56] A. Tofik, Abi M. Taddesse, T. Kebede, G. Goro, Fe-Al binary oxide nanosorbent: synthesis, characterization and phosphate sorption property, J. Environ. Chem. Eng. 4 (2016) 2458–2468.
[57] K. He, M. Li, L. Guo, Preparation and photocatalytic activity of PANI-CdS composites for H2 evolution, Int. J. Hydrog. Energy 37 (2012) 755–759.
[58] H. Katsumata, T. Hayashi, M. Taniguchi, T. Suzuki, S. Kaneco, Highly efficient visible light driven AgBr/Ag3PO4 hybrid photocatalysts with enhanced photocatalytic activity, Mater. Sci. Semicond. Process. 25 (2014) 68–75.
[59] C. Jin, G. Liu, L. Zu, Y. Qin, J. Yang, Preparation of Ag/Ag3PO4/ZnO ternary heterostructured for photocatalytic studies, Colloid Interface Sci. 453 (2015) 36–41.
[60] K. Lee, S. Cho, S.H. Park, A.J. Heeger, C.W. Lee, S.H. Lee, Metallic transport in polyaniline, Nature 441 (2006) 65–68.
[61] K. Wetchakuna, N. Wetchakunb, S. Sakulsermsuk, An overview of solar/visible light-driven heterogeneous photocatalysis for water purification: TiO2- and ZnO-based photocatalysts used in suspension photoreactors, J. Ind. Eng. Chem. 71 (2019) 19–49.
[62] H. Tedla, I. Diaz, T. Kebede, Abi M. Taddesse, Synthesis, characterization and photocatalytic activity of zeolite supported ZnO/Fe2O3/MnO2 nanocomposite, J. Environ. Chem. Eng. 3 (2015) 1586–1591.

[63] N.M. Dimitrijevic, B.K. Vijayan, O.G. Poluektov, T. Rajh, K.A. Gray, H. He, P. Zapol, Role of Water and Carbonates in Photocatalytic Transformation of CO2 to CH4 on Titania, J. Am. Chem. Soc. 133 (2011) 3964–3971.
[64] M. Pirhashemi, A. Habibi-Yangje, Photosensitization of ZnO by AgBr and Ag2CO3: Nanocomposites with tandem n-n heterojunctions and highly enhanced visible-light photocatalytic activity, J. Colloid Interface Sci. 474 (2016) 103–113.
[65] M. Shekofteh-Gohari, A. Habibi-Yangjeh, M. Abitorabi, A. Rouhi, Magnetically separable nanocomposites based on ZnO and their applications in photocatalytic processes: A review, Crit. Rev. Environ. Sci. Technol. 48 (2018) 10–12.